Controller Development for a Prototype High-Speed Low-Tension Tape Transport

Priyadarshee D. Mathur and William C. Messner, *Member, IEEE*

***Abstract*— This paper describes the entire process of control system design for a prototype tape spooler that is used for conducting research into the dynamics of high-speed and low-tension tape transport. This multiinput/multioutput (MIMO) system has interesting dynamics that make controller design a difficult, iterative process. The tape speed and tension are regulated by controlling the torque applied to the supply and the take-up reels. Each reel is directly driven by a motor, and no capstan is used. The system has slowly time-varying dynamics due to changing reel packs, but more challenging are dynamics associated with low-tension operation. The spooler operates near a hard nonlinearity, because the tape only supports positive tension. At low tension, air entrainment in between layers of tape in the take-up reel causes the effective spring constant of the tape to rapidly decrease during start-up. This paper begins with physical modeling of the transport and proceeds through iterative MIMO system identification and controller optimization. Adaptive tension ripple cancellation and fault detection and fault compensation are demonstrated. Experimental data are presented which demonstrate tape transport at 5 m/s with 0.28 N (1 oz.) tension and a start-up time of less than 150 ms.**

***Index Terms*— Digital tape transport, fault tolerance, identification, multivariable systems, ripple cancellation, tension control, velocity control, web transport.**

I. Introduction

FOR APPLICATIONS requiring mostly sequential data access, magnetic tape storage has provided a cost-effective alternative to disc-based storage systems since the 1950's. Unlike disc-based storage systems that have primarily relied on high *areal storage density* to achieve high *volumetric density*, tape systems have relied on their inherently high ratio of recording surface area to volume. Increasing areal storage density on tape requires reduction of the magnetic coating thickness [1], [2]. Simultaneously, very thin substrates are required to pack more tape in a given volume. Thus, low-tension transport is required to avoid tape damage. The data transfer rate is proportional to the linear density, the number of heads used to concurrently read and write data, and the linear velocity of the tape. High-performance tape drives, therefore, must rely on high-speed and low-tension tape transports for ultra-thin media.

Manuscript received February 13, 1996. Recommended by Associate Editor, M. Steinbuch. This work was supported in part by the National Science Foundation under Grant ECD-8907068 and the National Storage Industry Consortium.

P. D. Mathur is with the Department of Electrical and Computer Engineering, Carnegie Mellon University, Pittsburgh, PA 15213-3890 USA.

W. C. Messner is with the Department of Mechanical Engineering, Carnegie Mellon University, Pittsburgh, PA 15213-3890 USA.

Publisher Item Identifier S 1063-6536(98)04460-1.

TABLE I
CONTROLLER DESIGN SPECIFICATIONS FOR DIRECT-DRIVE TAPE TRANSPORT

Parameter	Specification
Media Thickness	
proposed	4 μm (157 μin)
used	10 μm (394 μin)
Operating speed	5 m/s ± 5% (200 in/s)
Start/stop time	150 ms
Operating tension	0.28 N ± 15% (1 oz.)
Peak tension	0.56 N (2 oz.)

This paper describes the design of a control system for a prototype tape spooler that is used for conducting research into the dynamics of high-speed and low-tension tape transport. This transport problem is related to the transport of webs, such as those used in the manufacture of paper, plastic, and sheet metal. The performance specifications for this transport are given in Table I. To reduce wear on the tape and to avoid the cost and bulk of added motors, vacuum units, and associated servos, the direct-drive transport (DDT) considered here uses only two independently driven reels to control the velocity and tension of the tape. The transport is inherently a multiinput/multioutput (MIMO) system. The requirement of the servo to provide rapid tape acceleration without relying on any buffering mechanism to protect the tape poses a difficult control system challenge. Small variations in the differential velocity of the winding rollers can cause large variations in tension [4], and for this reason, tension is measured by a strain gauge in the prototype rather than estimated from differential velocity measurements. The model of the DDT considered here resembles the model considered in [3]. Details of tape transport design are, otherwise, rare in the literature.

The dynamics of web transport are both nonlinear and time-varying. A web only supports positive tension, and ultra-low-tension operation takes place near this nonlinearity boundary. Time-varying dynamics arise because the radii and inertia of the winding rollers vary slowly during transport. Low-tension tape transport, in addition, has fast time-varying dynamics during start-up as air is entrained between layers of tape in the take-up reel. This reduces the effective spring constant of the tape because the unsupported tape span increases. Eccentricity in the rollers cause periodic disturbances in web tension during transport. In the prototype transport, this problem is particularly acute when the reel rotation frequencies are near the resonant frequency of the transport. These dynamics necessitated an iterative process of system identification and

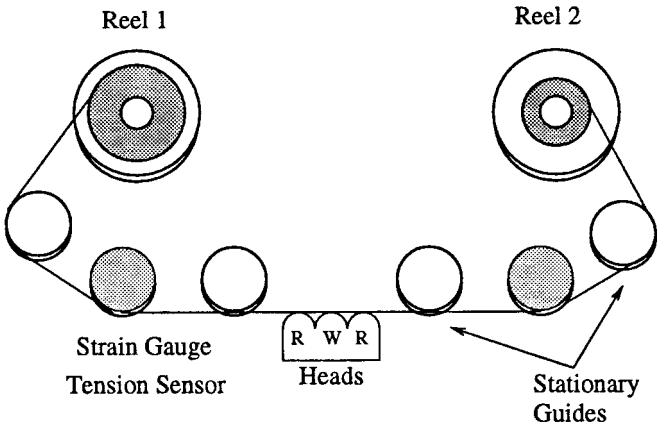

Fig. 1. Simplified layout of experimental tape transport.

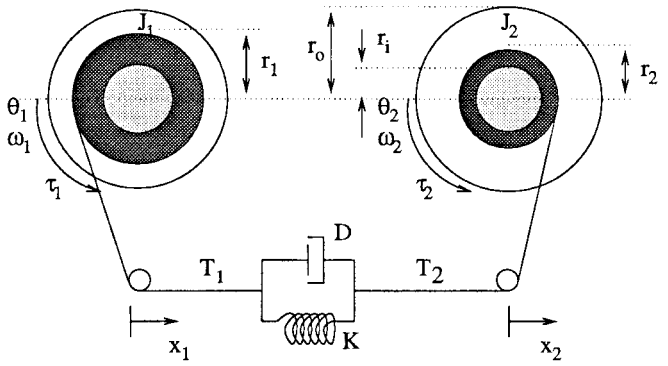

Fig. 2. Model of the experimental transport. Motor currents I_1 and I_2 (not shown) create torques τ_1 and τ_2, respectively. The tape tension is $T = T_1 = T_2$, assuming there is no force loss across the head.

controller design, including feedforward compensation for periodic tension ripple.

It is particularly important to incorporate fault detection and compensation into the prototype to protect the integrity of the media. The prototype is designed for easy access to electrical and mechanical components by users of the system. Consequently, the system is vulnerable to accidents such as disconnected cables, improperly threaded tape, or sticking of tape to the guides due to excess humidity, dirt, or improper handling. The control system uses an observer based scheme along with other tests for fault detection. Fault detection triggers an appropriate recovery algorithm that attempts to stop the tape while trying to maintain low tension.

This paper is organized as follows. In Section II, the hardware and modeling of the system is described. This model is simplified to a third-order linear model for controller design. In Section III, the iterative MIMO identification and control design process is described. In Section IV, an adaptive ripple cancellation (ARC) algorithm is designed to reduce tension ripple during transport. In Section V, fault detection mechanisms are described and demonstrated. Concluding remarks are in Section VI. Three appendices with notes on motor linearization, system identification, and implementation issues are included.

II. System Description and Modeling

A. Hardware Description

A schematic of the direct-drive prototype transport is shown in Fig. 1. The components of the DDT are mounted on a 1.9 cm (0.75 in) thick aluminum plate. Each reel is driven by one 100-W three-phase brushless motor obtained from Maxon Precision Motors Incorporated. The motors are driven by 150 W switching current amplifiers obtained from Western Servo Design Incorporated. Tension is sensed by one of two strain gauges located on guides posts that are in the path of the tape. The differential signals from the strain gauges are amplified using a 5000× instrumentation op-amp circuit. The tension sensing posts and the amplifier design were provided by Datatape Incorporated. Magnetic shields are wrapped around each motor to reduce flux-induced disturbances in the tension amplifier circuit. Angular position of each reel is measured by a 1024-line quadrature optical encoders obtained from US Digital Corporation. An LS7083 decoder operating in 4× mode allows position to be resolved into 4096 counts per revolution. Velocity is calculated by differentiating the encoder position rather than by measuring the time it takes for the encoder to increment or decrement one count. The former technique does not increase the interrupt load on the CPU as the velocity is increased. The quantization error from the differentiation is small (<0.4%) compared to the operating velocity for each reel.

B. Nonlinear Model

The schematic in Fig. 2 shows the parameters and state-variables of the system. The tape is modeled as a parallel spring and damper system. Each motor is modeled as a first-order system. Nonlinear friction dynamics around zero velocity are ignored in this analysis. However, a small bias compensation, described in Appendix A, was used to reduce their effects. The dynamics of the current amplifier were neglected after experimentally determining that the motor drivers could be modeled as a static gain of 1.5 A/V in the frequency range of interest (≤100 Hz).

The *state equations* for this system are derived as follows. Taking the derivative of the relation between reel radius $r(t)$ and angular position yields

$$\dot{r}_1(t) = -\epsilon\omega_1(t)/(2\pi) \tag{1}$$

$$\dot{r}_2(t) = \epsilon\omega_2(t)/(2\pi) \tag{2}$$

where ϵ is the thickness of the tape and $\omega(t)$ is the angular velocity of a reel. The inertia of each reel and their derivatives are a function of the reel radii

$$J(r(t)) = J_m + K_J\left(r^4(t) - r_i^4\right). \tag{3}$$

J_m is the sum of the inertia of the motor and the empty reel. The constant $K_J = t_\rho t_w \pi/2$, where t_ρ is the tape density and t_w is the tape width. The inner radius of the reel is denoted by the constant r_i.

The following equations are obtained because the sum of torques equals the change in angular momentum (the time

TABLE II
LIST OF SYSTEM PARAMETERS

Parameter	Value Used
t_ρ	1.607×10^3 Kg/m^3
Tape elastic modulus, t_{em}	8.29×10^9 N/m^2
ϵ	10 μm
t_w	8 mm
Unsupported tape length, t_l	$\approx$ 33 cm
$K = \epsilon t_{em} t_w / t_l$	2000 N/m
D	2 N s/m
r_i	9.75 mm
Outer reel radius, r_o	21.2 mm
J_m	103.5×10^{-7} Kg m^2
Inertia of reel n, J_n	$10 - 16 \times 10^{-6}$ Kg m^2
Kt	24.8×10^{-3} N m/Volt
β	1.03×10^{-4} N m s/rad

dependence is omitted for brevity)

$$\dot{J}_1\omega_1 + J_1\dot{\omega}_1 = Kt_1u_1 - \beta_1\omega_1 + Tr_1 \tag{4}$$

$$\dot{J}_2\omega_2 + J_2\dot{\omega}_2 = Kt_2u_2 - \beta_2\omega_2 - Tr_2. \tag{5}$$

The first term on the right-hand side is the applied torque from the motor, the second term is the torque due to viscous friction, and the third term is the torque resulting from the tape tension $T(t)$. Here, $u(t)$ is the voltage applied to a motor amplifier. The torque constant of a motor, including the gain of its motor driver, is denoted by Kt. The viscous friction coefficients of a motors is denoted by β. Differentiating (3) and substituting into (4) and (5) results in the following equalities:

$$\Rightarrow \dot{\omega}_1 = \frac{Kt_1u_1 - \beta_1\omega_1 + Tr_1 + 4\epsilon K_J r_1^3\omega_1^2 \,/\, (2\pi)}{J_1} \tag{6}$$

$$\Rightarrow \dot{\omega}_2 = \frac{Kt_2u_2 - \beta_2\omega_2 - Tr_2 - 4\epsilon K_J r_2^3\omega_2^2 \,/\, (2\pi)}{J_2}. \tag{7}$$

The tape stretch, $S(t)$, is given by

$$S(t) = S_0 + \int_{t_o}^{t} r_2(\tau)\omega_2(\tau)\,d\tau - \int_{t_o}^{t} r_1(\tau)\omega_1(\tau)\,d\tau \tag{8}$$

where $\int_{t_o}^{t} r(\tau)\omega(\tau)\,d\tau$ is the length of tape wound on a reel, and $S_0 \equiv S(t_0)$. The output equations for tension and linear tape velocity, $V(t)$, are given by

$$T(t) = KS(t) + D\dot{S}(t) \tag{9}$$

$$= KS + D(r_2\omega_2 - r_1\omega_1)$$

$$V(t) = \frac{1}{2}(r_1\omega_1 + r_2\omega_2) \tag{10}$$

where K and D are the spring constant and the damper coefficient of the tape. The state equation for tension is

$$\dot{T} = K(\omega_2 r_2 - \omega_1 r_1) + D(\dot{\omega}_2 r_2 - \dot{\omega}_1 r_1 + \omega_2 \dot{r}_2 - \omega_1 \dot{r}_1). \tag{11}$$

For the state vector $\mathbf{x} = [T \;\; r_1 \;\; r_2 \;\; \omega_1 \;\; \omega_2]^T$, the nonlinear state equations are given by (11), (1), (2), (6), and (7). The values and dimensions of the parameters used in the model are listed in Table II.

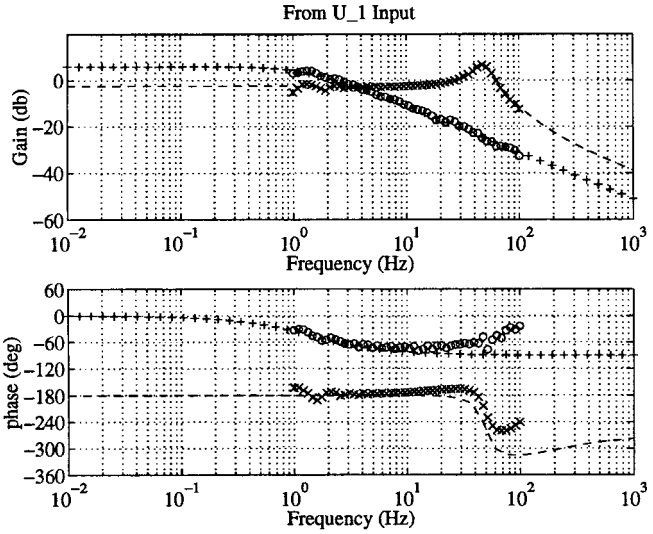

Fig. 3. Bode plots of third-order linear model for $r_1 \approx r_2$(velocity is "+"; tension is "−") from input u_1 are compared to frequency response obtained from nonlinear simulation (velocity is "o"; tension is "x"). Bode plots from input u_2 are similar, except that the phase of the tension output starts from 0° instead of -180°.

C. Simplification to Linear Model

Controller design is difficult for the nonlinear model derived above. Fortunately, several simplifications of the nonlinear model can be made. The most important simplification is to note that the dynamics for $r(t)$ are much slower than the dynamics for $\omega(t)$ and $T(t)$ because ϵ is very small. For small angular motion of the reels, the terms multiplying ϵ in the state equations can be neglected. Selecting $\mathbf{x} = [T \;\; \omega_1 \;\; \omega_2]^T$ as the state vector, and $\mathbf{y} = [V \;\; T]^T$ as the output vector, the following reduced order linear model is obtained:

$$\dot{\mathbf{x}}(t) = \mathbf{A}\mathbf{x}(t) + \mathbf{B}\mathbf{u}(t) \tag{12}$$

$$\mathbf{y}(t) = \mathbf{C}\mathbf{x}(t). \tag{13}$$

where

$$\mathbf{A} = \begin{bmatrix} -D\left(\frac{r_2^2}{J_2} + \frac{r_1^2}{J_1}\right) & -r_1K + \frac{D\beta_1 r_1}{J_1} & r_2K - \frac{D\beta_2 r_2}{J_2} \\ r_1/J_1 & -\beta_1/J_1 & 0 \\ -r_2/J_2 & 0 & -\beta_2/J_2 \end{bmatrix} \tag{14}$$

$$\mathbf{B} = \begin{bmatrix} -r_1Kt_1D/J_1 & r_2Kt_2D/J_2 \\ Kt_1/J_1 & 0 \\ 0 & Kt_2/J_2 \end{bmatrix} \tag{15}$$

$$\mathbf{C} = \begin{bmatrix} 0 & r_1/2 & r_2/2 \\ 1 & 0 & 0 \end{bmatrix}. \tag{16}$$

The frequency response of the nonlinear model around any set of operating radii was found to be in good agreement with the frequency response of the linear model (Fig. 3). Also, it was found that the resonant frequency of the tension output does not vary significantly with reel radii.

III. CONTROLLER DESIGN

Several controller design techniques were attempted. In general, controllers based on pole-placement using state-feedback

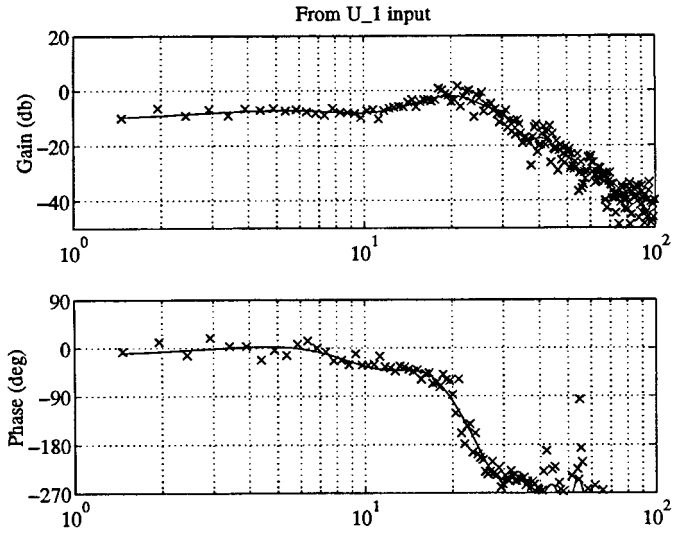

Fig. 4. Experimentally obtained Bode plots of tension output from both inputs for $r_1 = 13$ mm and $r_2 = 19$ mm at 5 m/s and 0.28 N operating point ("x" are the solutions to the least-squares estimation problem; the curve is the filtered average shown for clarity).

were found to be too sensitive to modeling errors; in implementation, a large gain from the velocity reference to the tension output was observed. The controller design presented below is based on the sequential loop closing (SLC) technique [5].

For SLC design, the system is described by a square transfer function matrix (TFM) and is assumed to be a set of (dominantly) decoupled SISO subsystems. One loop is closed at a time between one input and one output. As the loop is closed, the TFM of the remaining inputs to the outputs is reevaluated. This process is repeated until all the loops are closed. To avoid interaction between loops, it is generally wise to close the faster loops before closing the slower ones. Since stability of each loop is verified at each step, the resulting design is also *likely* to be stable. Hence, after the SLC design is complete, the designer must check the gain margin (GM) and phase margin (PM) of all loops by breaking one loop at a time.

The linear model derived in the previous section is radius dependent and not dominantly decoupled. A radius dependent decoupling scheme, described in Section III-A, was used to achieve dominant decoupling over the entire set of operating radii. A radii-*invariant* controller was then designed using SLC.

The first attempt to run the controller failed. However, by lowering the loop gains, it was possible to operate the transport and meet only the steady-state specifications, thus making it possible to perform multivariable system identification (see Appendix B). It was found that the dynamics of the tension loop were significantly different at run time. Fig. 4 shows that the resonant frequency is lowered at run time to 22 Hz and that the phase lag at the resonance is 128°, about 60° greater than expected. The resonant frequency shifting was attributed to air entrainment in the take-up reel, as it increased the unsupported tape length. The resonant frequency converges to the predicted value for high-tension low-speed transport, where intuitively one expects less air entrainment. The steep phase drop seen in the experimental data could be the result of a combination of propagation delays and unmodeled dynamics. Using the improved model, the tension loop was redesigned so that the controller could also meet the transient specifications. The SLC design procedure and experimental results for the improved controller are described in Section III-B.

A. Decoupling Scheme

Unlike in [4], where tension feedback is only applied to the take-up reel, using both motors to control both outputs improves tension transient response when the reference velocity is changed, as is often demanded in a tape transport. The TFM of the system is given by $\mathbf{G}(s) = \mathbf{C}(s\mathbf{I} - \mathbf{A})^{-1}\mathbf{B}$. By including a decoupling matrix, $\mathbf{De}$, at the plant input, $\mathbf{G}(s)\mathbf{De}$ is *dominantly* decoupled over the entire range of reel radii. SLC design can then be carried out on this new system.

The matrix $\mathbf{De}$ is found as follows. Assuming that the tape is very lightly damped, then $\dot{T}(t)$ depends mostly on the difference of the tangential velocity of each reel while the tape speed depends on their average. Therefore, to affect tension without affecting velocity, equal and opposite *linear* accelerations must be applied to each reel. At high frequencies ($\gg \beta/J$ rad/s), equal linear acceleration can be applied to affect speed without *significantly* affecting tension. The relations between $u_1(t)$ and $u_2(t)$ for each case are found by setting $\dot{\omega}_1(t)r_1(t) = \pm\dot{\omega}_2(t)r_2(t)$ in the linear model

$$\Rightarrow Kt_1u_1 - \beta_1\omega_1 + Tr_1 = \pm\frac{r_2J_1}{r_1J_2}(Kt_2u_2 - \beta_2\omega_2 - Tr_2). \tag{17}$$

Using the first term from each side of the equation, the simplified weighting scheme using only input premultiplication was found to be satisfactory

$$\Rightarrow u_1(t) \approx \frac{Kt_2r_2J_1}{Kt_1r_1J_2}u_2(t). \tag{18}$$

These results are used to decouple the system by premultiplying the input by the matrix $\mathbf{De}$. Assuming $Kt_1 = Kt_2$ (i.e., the motors are matched)

$$[u_1 \quad u_2]^T = \underbrace{\begin{pmatrix} r_2J_1/r_1J_2 & -r_2J_1/r_1J_2 \\ 1 & 1 \end{pmatrix}}_{\mathbf{De}}[v_i \quad t_i]^T. \tag{19}$$

Here, $v_i(t)$ and $t_i(t)$ are the velocity and tension control inputs into the dominantly decoupled plant. Fig. 5 shows that the decoupling is perfect at mid-pack. Decoupling breaks down at low frequency as the difference in reel radii increases. Decoupling at DC is not necessary, as integrators are used in each loop for zero steady-state error to a step.

B. SLC Design Using Experimental Data

The tension loop from $t_i(t)$ to $T(t)$ was closed first with as high a bandwidth as possible. A notch filter was used to remove the resonance seen in Fig. 4. Another notch filter was added at the average of the reel rotation frequencies (≈59 Hz) to reduce sensitivity to disturbances arising from

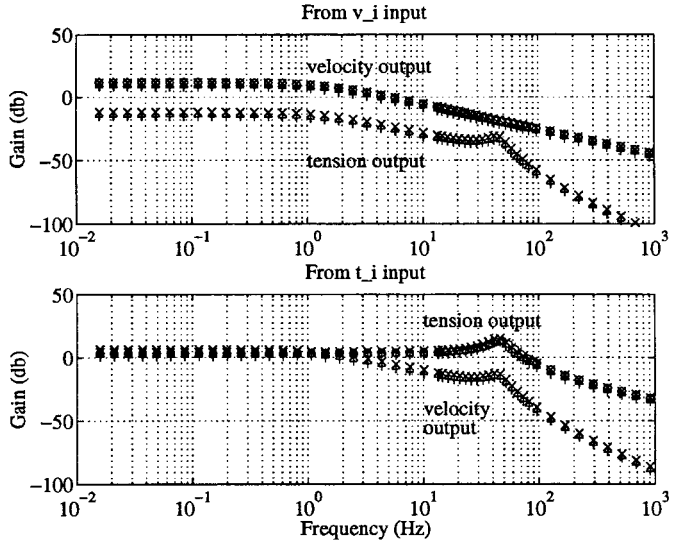

Fig. 5. Bode magnitude plots from v_i and t_i inputs to both outputs at equal packs ("o"), reel 1 empty ("x"), and reel 1 full ("+").

reel eccentricity and also to add phase at that frequency. An integrator was added to maintain zero steady-state error to a step. Finally, a first-order lead was included to add about 20° phase at 125 rad/s (20 Hz). The tension loop compensator is given by (20). The PM is about 45° at a crossover frequency of 113 rad/s (18 Hz)

$$z_1 = -22.3 \cdot 2\pi(0.1 + j)$$
$$z_2 = -58.9 \cdot 2\pi(0.2 + j)$$
$$C_{\text{ten}} = 130 \frac{\left(\frac{s}{-z_1} + 1\right)\left(\frac{s}{-z_1^*} + 1\right)}{s\left(\frac{s}{1500} + 1\right)} \cdot \frac{\left(\frac{s}{-z_2} + 1\right)\left(\frac{s}{-z_2^*} + 1\right)}{\left(\frac{s}{1200} + 1\right)^2} \frac{\left(\frac{s}{87.5} + 1\right)}{\left(\frac{s}{179} + 1\right)}. \quad (20)$$

Fig. 6 shows the Bode plots from $t_{\text{ref}}(t)$ and $v_i(t)$ to both outputs, calculated using the relation

$$\begin{bmatrix} V \\ T \end{bmatrix} = \begin{bmatrix} d_{11} - \frac{d_{12}d_{21}C_{\text{ten}}}{1+d_{22}C_{\text{ten}}} & \frac{d_{12}C_{\text{ten}}}{1+d_{22}C_{\text{ten}}} \\ \frac{d_{21}}{1+d_{22}C_{\text{ten}}} & \frac{d_{22}C_{\text{ten}}}{1+d_{22}C_{\text{ten}}} \end{bmatrix} \begin{bmatrix} v_i \\ t_{\text{ref}} \end{bmatrix} \quad (21)$$

where $d_{ij}(s)$ are the components of $\mathbf{D}(s) = \mathbf{G}(s)\mathbf{De}$.

Next, the velocity loop was closed using the proportional-integral (PI) controller given by (22), resulting in a gain-crossover frequency of about 36 rad/s (5.7 Hz). The GM and PM of each loop were evaluated with the other loop closed

$$C_{\text{vel}} = 10\frac{(s/10 + 1)}{s}. \quad (22)$$

The controller designed above was implemented at a sampling rate of 500 Hz. The z-transform of each biquadratic term in the filter designed above was computed by frequency prewarping at its notch frequency. The results were then cascaded to obtain a good approximation of the analog filter. A raised cosine curve from 0 to (±) 5.08 m/s was used for the velocity reference to reduce transients in the outputs. The tension reference was a constant 0.28 N.

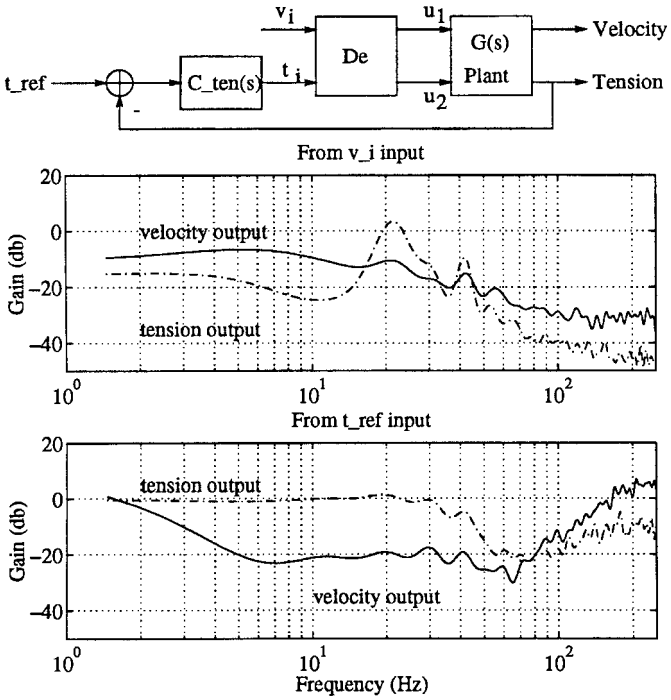

Fig. 6. Bode magnitude plots from v_i and t_{ref} inputs to both outputs when $r_1 = 13$ mm and $r_2 = 19$ mm (calculated from experimental data; trends plotted for clarity).

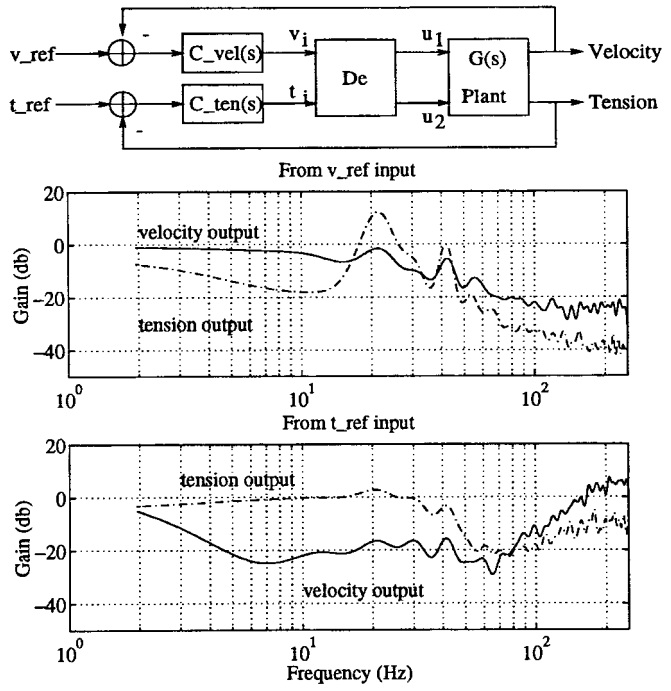

Fig. 7. Bode magnitude plots from v_{ref} and t_{ref} inputs to both outputs when $r_1 = 13$ mm and $r_2 = 19$ mm (calculated from experimental data; trends plotted for clarity).

During start-up, the velocity loop gain was doubled to reduce the velocity settle time. Increasing the gain in steady-state only increased the sensitivity of the tension output to noise, hence the velocity loop gain was reduced back to half of the gain used during start-up. Fig. 7 shows the Bode plots for the system when both loops are closed and the velocity loop gain is doubled.

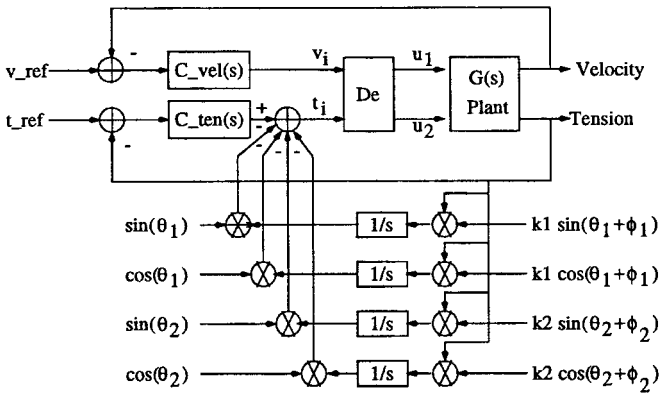

Fig. 8. Feedforward structure of adaptive ripple compensation.

The controller was capable of reliable operation over the entire span of reel radii. However, the tension output exhibited a limit-cycle behavior when the transport was stopped because of nonlinear friction arising from contact at the guides. This problem was fixed by reducing the gain of the tension loop by a factor of four when the drive was stopped. Similarly, once the drive had settled, the gain of the tension loop was reduced to decrease sensitivity to noise. With these modifications, the transport could be operated reliably and meet the specifications in Table I.

IV. Adaptive Ripple Cancellation (ARC)

When the compensator designed above was implemented, ripple in the tape tension was observed at the rotation frequency of each reel. Fig. 9(a) shows these components along with the component from the plant resonance. Such ripple may be caused by tape eccentricity or bias errors in the motor driver circuits. Tension ripple can cause bits of unequal lengths to be written on the tape. At high recording density, data synchronization can become a problem.

To reduce this disturbance, we considered the feedforward algorithm considered in [6]. This structure was selected over the internal model-based compensator structure because the latter requires the functions $1/(s+\omega_i^2), i = 1, 2$ to be included in the compensator, but ω_i vary as the *linear* velocity of the tape is held constant. Correlating the disturbance with θ_i in the feedforward algorithm is more intuitive. Also, the feedforward approach can be momentarily suspended when the drive is at rest or in a start to stop transition where the tension output is not accurately determined, even by the nonlinear model of the system. The structure of the ARC is shown in Fig. 8. For maximum phase margin, the regressor phase, ϕ_i (see Fig. 8), must be set to the phase of the plant from the corresponding input at the disturbance frequency. The system is stable only when ϕ_i is within $\pi/2$ rad of the plant phase and the adaptation gain is sufficiently small [6].

The disturbance frequency changes as the radii vary, and the frequency response of the plant itself depends on the speed and tension in steady-state operation. Even if an experimental frequency response plot is obtained for a particular operating velocity and tension, some gain scheduling would be required to set ϕ_i as a function of the radii. Such an extensive gain-scheduling method has not been implemented yet, but the algorithm is shown to reduce tension ripple around a chosen set of operating radii.

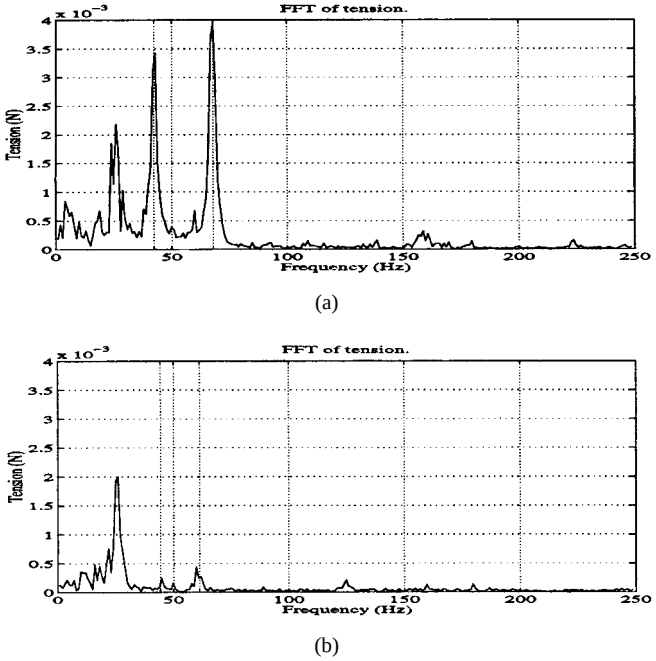

Fig. 9. (a) Two largest components of tension ripple are at the rotation rate of each reel. (b) Ripple in steady-state when ARC is used.

Implementing this algorithm on the DDT is difficult because the phase of the plant cannot be easily determined beyond 30 Hz. For this experiment, however, the phase of the plant was determined by manually setting each ϕ and searching for the two corresponding instability boundaries. The actual phase of the plant is the close to average of these two measurements. It should be noted that the phase of the plant from each reel is different depending on the direction of motion for a given pair of operating radii. This is because air-entrainment occurs only on the take-up reel, thereby increasing the length of the tape path to the tension sensor, and hence the propagation delay.

The ARC algorithm was implemented with $\phi_1 = 44°$, $k_1 = 0.06$, $\phi_2 = 180°$, and $k_2 = 0.06$ for reel-2 full and tape-up on reel-1. Fig. 9(b) shows that the two tension ripple components associated with the rotation rate of the reels are practically eliminated. The peak associated with the resonance remains around the same value obtained when no ARC is used.

To isolate the effect of the ARC algorithm, performance of the controller is compared with and without ARC. For multiple test runs, the standard deviation of the tension ripple was typically reduced by 0.007 N (58% of ripple). The maximum and minimum tension deviation recorded in *steady-state* decreased by 0.011 N (43% of ripple) and 0.014 N (52% of ripple) respectively. As expected, the settle time of the tension loop at start-up decreased by only 9 ms, since ARC cannot reduce tension ripple arising from the transient behavior of the air bearing. Fig. 10 shows a typical run when ARC was enabled.

V. Fault Tolerance and Implementation Issues

In any data storage device, the user data and media are considered sacred. To reduce the risk of media damage, the

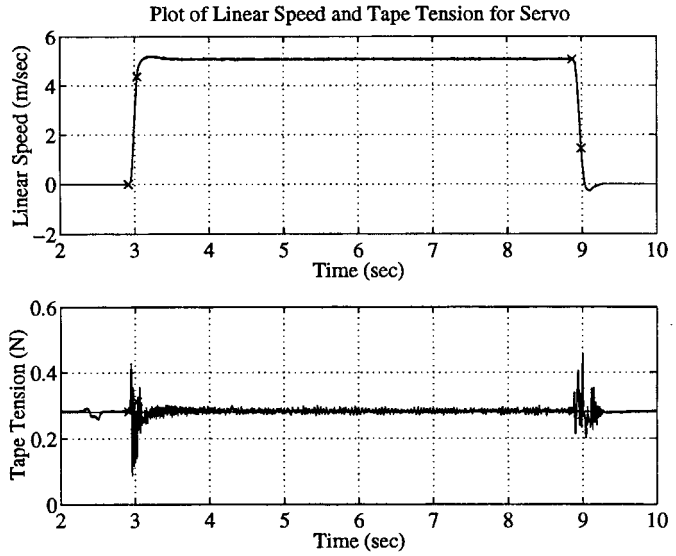

Fig. 10. Experimental results when tape is transported and ARC is used.

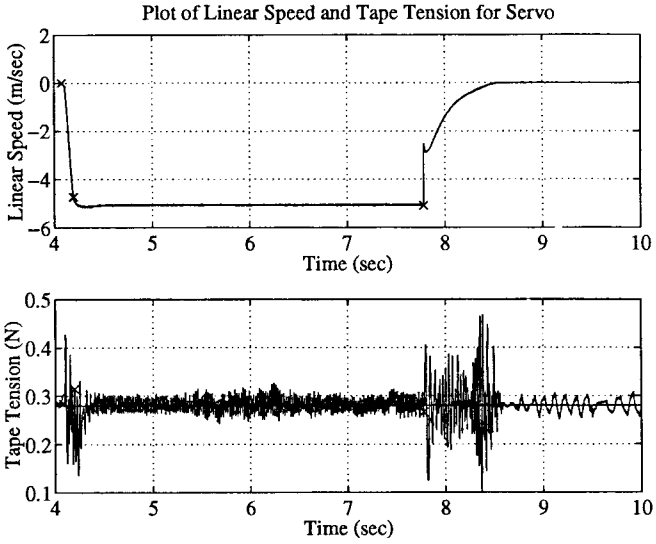

Fig. 11. Velocity feedback is corrupted by disconnecting one encoder. Note that the tension is maintained while the drive is stopped. ARC was switched off for this particular experiment.

following tests were implemented during drive initialization and during run time.

A. Initialization Tests

Before drive operation begins, it is important to verify that the tape is threaded correctly and that at least the static response of the system is within expected bounds.

During drive initialization, both motor currents are set to zero and the system is allowed to settle. After that, a nonzero tension is indicative of stiction between the tape and the guides or measurement offset error. If the system passes this test, the motor currents are slowly ramped, but with opposite polarity. If the tension does not increase linearly, it could indicate that tension feedback is unavailable because the tape is broken or not threaded, or because the tension amplifier is malfunctioning. If the system passes the second test, the tape is slowly spooled open-loop for about a quarter of a revolution, but without exceeding the tension specifications of the tape. Reel radii are estimated during this time.

If the drive failed these initialization tests, the user would be informed of the failure.

B. Run Time Tests

During run time, the control system checks to ensure that the tape does not slack for over 20 ms or that the peak tension does not exceed 0.6 N. If either of these conditions occurs, both reels are stopped independently in under 60 ms using two proportional controllers. These simple checks can detect a slowly growing instability. Also, if there is excess tape stiction to the guides, the higher tension transients during start-up would trigger these checks.

In addition to these checks, a reduced order observer is used to ensure that motor dynamics are within expected bounds. Unfortunately, the lack of an accurate model for determining tension makes it difficult to predict tension for fault detection. Since tension is measured, the reduced order observer is given by

$$\dot{\hat{\mathbf{x}}}_c(t) = \mathbf{A}_c\hat{\mathbf{x}}_c(t) + \mathbf{B}_c\mathbf{u}_c(t) + \mathbf{L}_c(\mathbf{x}_c(t) - \hat{\mathbf{x}}_c(t)) \tag{23}$$

where

$$\mathbf{x}_c = [\omega_1 \quad \omega_2]^T \tag{24}$$

$$\mathbf{u}_c = [u_1 \quad u_2 T]^T \tag{25}$$

$$\mathbf{A}_c = \begin{bmatrix} -\beta_1/J_1 & 0 \\ 0 & -\beta_2/J_2 \end{bmatrix} \tag{26}$$

$$\mathbf{B}_c = \begin{bmatrix} Kt_1/J_1 & 0 & r_1/J_1 \\ 0 & Kt_2/J_2 & -r_2/J_2 \end{bmatrix} \tag{27}$$

and $\mathbf{L}_c$ is the observer gain matrix. For implementation, this observer must be converted to a digital model assuming a zero-order hold on the plant inputs. The discrete-time observer was implemented with poles $p_1 = p_2 = 0.9$ and $T = 0.002$ s.

During run time, if estimates of the velocity are over 10% in error compared to the measurements, a two-step algorithm is used to stop the transport. First, the $v_i(t)$ input is exponentially decreased by the rule $v_i[k+1] = 0.95v_i[k]$. During this time, the tension controller is allowed to operate. At low-tension operation, friction in the system is sufficient to stop the transport when $v_i(t) = 0$. If during this recovery algorithm, the tape slacks or the tension exceeds safe bounds, then the $t_i(t)$ input is also set to zero. The transport stops due to its natural damping, but tape may fall off the guides during this process, even though it is not destroyed.

Fig. 11 shows a sample run when one encoder wire was disconnected while the drive was operating. The corrupted velocity feedback was detected by the observer and the transport was stopped without losing tension control. ARC was not enabled during this test. These error traps significantly reduced tape waste during controller development, and also made the drive reliable enough for other researchers to use this transport through a mouse driven user interface written in object oriented Turbo Pascal.

VI. Remarks and Future Work

This paper has addressed many practical issues involved in high-speed and low-tension transport. Problems with complicated dynamics associated with air-entrainment and system delays were identified and solutions were incorporated into the control system design. While the focus of this paper has only been 5 m/s operation at 0.28 N, the ideas presented here, with the exception of ARC, have been used to design controllers for several operating points. An ARC scheme to reduce tension ripple during transport was also demonstrated for a small operating region. Finally, fault detection and compensation methods were described.

Faster controller implementation on, e.g., a digital signal processor, might allow for online identification of the system frequency response, at least at the reel rotation frequencies. This data could be used to set the ϕ_i parameters in the ARC block automatically. Better understanding of air entrainment dynamics and stiction may be gained from the use of this system. This knowledge could be used to develop special compensators for improving transient response.

Appendix A
Compensation for Motor Static and Coulomb Friction

A compensation scheme to reduce nonlinear dynamics of the dc motors is presented. For this section, note that both reels are empty and the tape is not threaded. Furthermore, both motors were matched on the prototype, hence only one set of compensation parameters was needed. Compensation was applied for both static friction and Coulomb friction.

A deadzone is observed when the steady-state angular velocity of one of the motors is plotted versus a step $u(t)$ to the motor driver input. This deadzone increases the settle time of the controller when starting from rest. To compensate for multivalued friction when the motor speed is within some threshold $\omega_{\rm th}$ around zero velocity, a small bias given by (28) is applied

$$v_{\rm bs}(t) = v_{\rm dz}\,\mathrm{sgn}(u(t)), \qquad \text{for } |\omega(t)| < \omega_{\rm th}. \tag{28}$$

Here, $v_{\rm dz}$ are the widths of the deadzone measured for each motor (about 73 mV for the motors used).

So far, the first two terms on the right-hand side of (29) were used to linearly model each motor. The Coulomb friction term, with C (Nm) coefficient, was neglected

$$J_m\dot{\omega}(t) = Ktu(t) - \beta\omega(t) - C\,\mathrm{sgn}(\omega(t)). \tag{29}$$

To compensate for Coulomb friction, C and Kt must be identified, and $v_{\rm bc}(t) = C\,\mathrm{sgn}(\omega(t))/Kt$ must be applied when $|\omega(t)| \geq \omega_{\rm th}$. However, in a dc brushless motor, C is small and identifying it using least squares algorithms in the presense of noise is difficult. Therefore, a trial and error approach for finding C was used. By combining this result with (28), the following biasing scheme was obtained:

$$v_{\rm bias}(t) = \begin{cases} 73.2\,\mathrm{sgn}(u(t)), & \text{for } \omega(t) < 7.12 \text{ rad/s} \\ 61.0\,\mathrm{sgn}(\omega(t)), & \text{otherwise} \end{cases} \text{mV}. \tag{30}$$

When the motor is at rest, the static friction responsible for keeping the motor at rest equals the torque resulting from the applied current, until a breakaway threshold is exceeded. Applying $v_{\rm bs}(t)$ maintains the operating point of the motor at one of the breakaway points, depending on the direction of current applied. When the motor starts moving, direction-dependent Coulomb friction and viscous friction act together to oppose the motion of the motor. Applying a direction dependent bias $v_{\rm bc}(t)$ reduces the effects of nonlinear Coulomb friction. The resulting apparent friction is approximately linear with velocity.

Appendix B
Multivariable System Identification Procedure

The frequency response of the DDT is generated by solving for the TFM $\mathbf{G}(s)$ from input-output data. For a two-input/two-output system, at least two data sets are needed to find a solution. More data sets may be used for better averaging. Each data set is taken around the same radius and at the same operating speed and tension, which are maintained in closed-loop. For a total of N data sets, the discrete-time Fourier transform (DTFT) of the input and output measurements is taken. The transformed input–output data are written as a function of the unknown TFM

$$\underbrace{\left[\mathbf{Y}(j\omega)^{\langle 1\rangle} \vdots \mathbf{Y}(j\omega)^{\langle 2\rangle} \vdots \cdots \vdots \mathbf{Y}(j\omega)^{\langle N\rangle}\right]}_{\Phi} = \mathbf{G}(j\omega) \cdot \underbrace{\left[\mathbf{U}(j\omega)^{\langle 1\rangle} \vdots \mathbf{U}(j\omega)^{\langle 2\rangle} \vdots \cdots \vdots \mathbf{U}(j\omega)^{\langle N\rangle}\right]}_{\Psi}. \tag{31}$$

Here, $Y(j\omega) = [V(j\omega)\ T(j\omega)]^T$ and $U(j\omega) = [u_1(j\omega)\ u_2(j\omega)]^T$. The TFM is computed using a pseudoinverse $\mathbf{G}(j\omega) = \Phi(j\omega)\Psi(j\omega)^T(\Psi(j\omega)\Psi(j\omega)^T)^{-1}$.

For meaningful solutions to exist, the power spectrum of the input must be greater than zero at each frequency. To meet this condition, random noise was injected into both inputs. However, there is a limit on the amount of noise injected into the inputs because very small disturbances can change the tape tension drastically. The strength of the injected noise was carefully increased until the tension variation was about 20% of the nominal 0.28 N. Such small disturbances barely affect the velocity output. Hence, the frequency response of the velocity output is difficult to obtain. However, this insensitivity also indicates that the velocity loop can be designed independently from the tension loop.

Since the reel radii change as the tape is transported, each data set was limited to about 2 s. The sampling frequency was 500 Hz and 1024 samples were collected for the DTFT. Thus, the frequency resolution was about 0.5 Hz. A total of 20 data sets were used to solve for the frequency response of the system. To obtain the frequency response of the nonlinear model in Section II-B, input–output data was gathered from simulations done using SIMULINK™.

APPENDIX C
RADIUS COMPUTATION

In the discussion so far, it has been assumed that the reel radii were known for computing the $\mathbf{De}$ matrix. In the absense of a functional read channel for linear tape speed feedback, we used approach based on the observation that the total cross-sectional area of the tape is conserved as it is spooled from one reel to the other. This is true if there is no slack in the tape and if the length of tape between the two reels is constant. By noting the initial reel radii, r_{1o} and r_{2o}, once prior to drive operation, the reel radii at any point in time can be computed by (34). This method allows the radii to be computed even when ϵ is not known. Radius is updated only if the tension is positive and if the reels are rotating. Substituting (33) into (32) leads to (34)

$$\pi r_{1o}^2 + \pi r_{2o}^2 = \text{const} = \pi\left(r_1^2 + r_2^2\right) \tag{32}$$

$$r_2 = \frac{\omega_1}{\omega_2} r_1 \tag{33}$$

$$\Rightarrow r_1 = \sqrt{\frac{r_{1o}^2 + r_{2o}^2}{\frac{\omega_1^2}{\omega_2^2} + 1}}. \tag{34}$$

ACKNOWLEDGMENT

The authors would like to acknowledge Dr. M. Bodson under whom this project was started and Datatape Incorporated for donating equipment and expertise.

REFERENCES

[1] R. E. Matick, *Computer Storage Systems and Technology*. New York: Wiley, 1977.
[2] C. D. Mee and E. D. Daniel, *Magnetic Recording Handbook: Technology and Applications.* New York: McGraw-Hill, 1990.
[3] G. F. Franklin, J. D. Powell, and E. Abbas, *Feedback Control of Dynamic Systems*. Reading, MA: Addison-Wesley, 1986.
[4] G. E. Young and K. N. Reid, "Lateral and longitudinal dynamic behavior and control of moving webs," *Trans. ASME: J. Dynamic Syst., Measurement, Contr.*, vol. 115, no. 20B, June 1993.
[5] J. M. Maciejowski, *Multivariable Feedback Design*. Reading, MA: Addison-Wesley, 1991.
[6] W. Messner and M. Bodson, "Design of adaptive feedforward algorithms using internal model equivalence," *Int. J. Adaptive Contr. Signal Processing*, vol. 9, 1995.

Priyadarshee D. Mathur received the B.S. degree in electrical engineering from the University of Maryland, College Park, in 1993. Since then, he has been a graduate student at the Electrical and Computer Engineering department at Carnegie Mellon University, Pittsburgh, PA.

He completed his M.S. project on multivariable controller design for a direct drive tape transport in December 1994 and is currently investigating servo issues for high-density disc drives. This work includes modeling of the position error signal generation process and design of control algorithms that take into account models of disturbance and noise encountered inside a drive.

William C. Messner (S'89–M'91) was born and raised in Massachusetts. He received the B.S. degree in mathematics from the Massachusetts Institute of Technology, Cambridge, in 1985. He received the M.S and Ph.D. degrees in mechanical engineering from the University of California at Berkeley in 1989 and 1992, respectively. His graduate work was conducted under the supervision of Dr. Roberto Horowitz in the theory and application of linear integral transforms for learning and repetitive control problems.

He worked for BBN Laboratories, Newport, RI, from 1985 to 1987. He joined the Department of Mechanical Engineering at Carnegie Mellon University, Pittsburgh, PA, in 1993, where he now leads the servo control research effort for the Data Storage Systems Center (DSSC), an NSF Engineering Research Center.

Dr. Messner received Carnegie Mellon's George Tallman Ladd Award for Excellence in 1996. More recently he was a recipient of the 1997 ASME/EDUCOM Medal for the development information technologies for education, and he was a finalist for the Best Paper Award at the 1997 International Conference on Robotics and Automation.